

## Pressure tuning of structure, magnetic frustration, and carrier conduction in the Kitaev spin liquid candidate $\text{Cu}_2\text{IrO}_3$

Srishti Pal <sup>1,\*,\dagger</sup>, Pallavi Malavi <sup>1,\*,\ddagger</sup>, Arijit Sinha <sup>2</sup>, Anzar Ali,<sup>3</sup> Piyush Sakrikar,<sup>3</sup> Bobby Joseph <sup>4</sup>, Umesh V. Waghmare,<sup>2</sup> Yogesh Singh <sup>3</sup>, D. V. S. Muthu,<sup>1</sup> S. Karmakar <sup>5</sup> and A. K. Sood <sup>1</sup>

<sup>1</sup>Department of Physics, Indian Institute of Science, Bengaluru 560012, India

<sup>2</sup>Theoretical Sciences Unit, Jawaharlal Nehru Centre for Advanced Scientific Research, Bengaluru 560064, India

<sup>3</sup>Department of Physical Sciences, Indian Institute of Science Education and Research (IISER) Mohali, Knowledge City, Sector 81, Mohali 140306, India

<sup>4</sup>Elettra-Sincrotrone Trieste S.C. p.A., S.S. 14, Km 163.5 in Area Science Park, Basovizza 34149, Italy

<sup>5</sup>HP&SRPD, Bhabha Atomic Research Centre, Trombay, Mumbai 400085, India



(Received 11 May 2022; revised 11 November 2022; accepted 24 January 2023; published 6 February 2023)

The layered honeycomb lattice iridate  $\text{Cu}_2\text{IrO}_3$  is the closest realization of the Kitaev quantum spin liquid, primarily due to the enhanced interlayer separation and nearly ideal honeycomb lattice. We report pressure-induced structural evolution of  $\text{Cu}_2\text{IrO}_3$  by powder x-ray diffraction (PXRD) up to  $\sim 17$  GPa and Raman scattering measurements up to  $\sim 25$  GPa. A structural phase transition (monoclinic  $C2/c \rightarrow$  triclinic  $P\bar{1}$ ) is observed with a broad mixed phase pressure range ( $\sim 4$  to 15 GPa). The triclinic phase consists of heavily distorted honeycomb lattice with Ir-Ir dimer formation and a collapsed interlayer separation. In the stability range of the low-pressure monoclinic phase, structural evolution maintains the Kitaev configuration up to 4 GPa. This is supported by the observed enhanced magnetic frustration in dc susceptibility without emergence of any magnetic ordering and an enhanced dynamic Raman susceptibility. High-pressure resistance measurements up to 25 GPa in the temperature range 1.4–300 K show resilient nonmetallic  $R(T)$  behavior with significantly reduced resistivity in the high-pressure phase. The Mott 3D variable-range-hopping conduction with much reduced characteristic energy scale  $T_0$  suggests that the high-pressure phase is at the boundary of localized-itinerant crossover. First-principles density functional theoretical (DFT) analysis shows that monoclinic  $P2_1/c$  phase of  $\text{Cu}_2\text{IrO}_3$  is energetically lower than its  $C2/c$  phase at ambient pressure and both the structures are consistent with experimental XRD pattern. Our analysis reveals structural transition from  $P2_1/c$  to  $P\bar{1}$  structure at 7 GPa in agreement with experiment and uncovers the interplay between oxidation states, spin, Ir bond dimerization and their relevance to electronic band gap.

DOI: [10.1103/PhysRevB.107.085105](https://doi.org/10.1103/PhysRevB.107.085105)

### I. INTRODUCTION

In the last decade, for possible experimental realizations of Kitaev quantum spin liquid (QSL) ground states [1,2], the quasi-two dimensional (2D) honeycomb iridates and ruthenates have attracted tremendous research interest [3–11]. In these  $d^5$  systems, presence of strong spin-orbit coupling (SOC) leading to pseudo spin  $J_{\text{eff}} = 1/2$  and the edge-sharing octahedral network gives rise to anisotropic Ising exchange interaction, the key ingredient of the Kitaev model [1]. The prime candidates for this model suffer from the concomitant isotropic Heisenberg exchange (often beyond nearest neighbor) and the off-diagonal exchange components (due to nonideal honeycomb lattice), resulting in undesired long-range magnetic order at low temperature, viz., the zigzag antiferromagnetic (AFM) order in  $\text{Na}_2\text{IrO}_3$  [3],  $\alpha\text{-RuCl}_3$  [8], and incommensurate spiral AFM order in  $\alpha\text{-Li}_2\text{IrO}_3$  [11].

However, the observation of fractional magnetic excitations in neutron, Raman, and resonant inelastic x-ray scattering measurements have firmly established these materials as proximate quantum spin liquid systems [9,12–14]. Efforts to bring the candidate materials closer to Kitaev limit by suppressing the magnetic order have been successful by isoelectronic cation doping [15,16] and by application of magnetic field [17–19]. In comparison, similar efforts to tune the various exchange interactions by tuning the crystal structure through application of external pressure have not been successful for these compounds. The 2D honeycomb lattice undergoes distortion even at a moderate pressure leading to Ir-Ir dimer formation [20–24], that either destroys the  $\text{Ir}^{4+} J_{\text{eff}} = 1/2$  configuration [20] or causes magnetic collapse with emergence of a spin-singlet VBS state [21,22]. While  $\text{Na}_2\text{IrO}_3$ ,  $\alpha\text{-Li}_2\text{IrO}_3$ , and  $\alpha\text{-RuCl}_3$  exhibit resilient nonmetallic character up to very high pressures, the significant drop in resistivity in the high-pressure phases hints for drastic electronic structural modification with possible insulator-metal crossover [25–27].

In a novel approach to reach the Kitaev limit by replacing the honeycomb iridate interlayer octahedra by dumbbells has led to the synthesis of a new class of compounds,  $\text{Cu}_2\text{IrO}_3$ ,  $\text{H}_3\text{LiIr}_2\text{O}_6$ , and  $\text{Ag}_3\text{LiIr}_2\text{O}_6$  [28–30]. Although the

\*These authors contributed equally to this work.

<sup>\dagger</sup>srishtipal@iisc.ac.in

<sup>\ddagger</sup>Part of this work was conducted by P.M. during her visit to Bhabha Atomic Research Centre, Trombay, Mumbai 400085, India.

structural modifications in these materials result in  $\sim 20 - 30\%$  enhanced interlayer separation and more ideal honeycomb configuration, all of these compounds are prone to disorders. While structural disorder in  $\text{Ag}_3\text{LiIr}_2\text{O}_6$  is synthesis related with a scope to improve [31], interlayer proton disorder in  $\text{H}_3\text{LiIr}_2\text{O}_6$  [32–35] and presence of mixed valent  $\text{Cu}^+/\text{Cu}^{2+}$  within intralayer  $\text{CuO}_6$  octahedra [36,37] are of fundamental nature. Interestingly, recent advances to explore the nature of the ground state in  $\text{Cu}_2\text{IrO}_3$  have confirmed that the  $\text{Cu}^{2+}$  impurity spins, 5% in present batch of samples [38], only nucleate regions of random singlet states, which are phase separated from the dynamically fluctuating QSL background ( $\sim 90\%$  of the total sample volume) [36,37]. Moreover, the spin-liquid nature of the ground state of this material has been further substantiated by the observed fractional excitations in Raman scattering and NQR measurements [38,39]. More recently, optical phonons renormalization below the Kitaev temperature scale of  $\sim 120$  K has been quantitatively attributed to the interaction of phonons with the Majorana fermions [38]. Recent high-pressure studies on the  $\text{Cu}_2\text{IrO}_3$  system [40,41] have detected two pressure-induced structural transitions at  $\sim 7$  GPa and 11–15 GPa. While the first transition is reported to be to a triclinic  $\alpha - P\bar{1}$  followed by Ir-Ir dimerization, the high-pressure structure after the second transition was only predicted by DFT based evolutionary structure search method and could not be uniquely determined by a successful refinement of the PXRD pattern. Interestingly, high-pressure resistivity measurements on this system [41] have shown that the second structural transition is associated with an insulator to metal transition. However, DFT calculations [40] could not capture the same and predicted opening up of a gap of  $\sim 0.3$  eV in the dimerized phase. Hence, the effect of hydrostatic pressure in this proximate Kitaev QSL candidate is yet to be examined thoroughly, thus motivating this present study.

We report here the structural, vibrational, magnetic, and electronic properties of  $\text{Cu}_2\text{IrO}_3$  up to  $\sim 25$  GPa using a combination of PXRD, Raman scattering, magnetic susceptibility, resistivity measurements, and density functional theoretical calculations. A structural phase transition (monoclinic  $C2/c \rightarrow$  triclinic  $P\bar{1}$ ) is observed in a broad mixed-phase pressure range ( $\sim 4$  to 15 GPa). The triclinic phase consists of heavily distorted honeycomb lattice with Ir-Ir dimer formation and a collapsed interlayer separation. In the stability range of the low-pressure monoclinic phase (up to  $\sim 4$  GPa), structural evolution with pressure drives the system marginally towards the Kitaev limit. This is further supported by the observed enhanced magnetic frustration in dc susceptibility without emergence of any magnetic ordering and an enhanced dynamic Raman susceptibility. High-pressure resistance measurements show resilient nonmetallic temperature dependence up to 25 GPa, but with significantly reduced resistivity in the high-pressure phase. The Mott 3D variable-range-hopping conduction with much reduced characteristic energy  $T_0$  indicates enhanced density of states at Fermi level suggesting the high-pressure phase to be at the boundary of localized-itinerant crossover. Our DFT calculations capture a pressure dependent structural transition at  $\sim 7$  GPa from  $P2_1/c$  to  $P\bar{1}$  structure, which involves dimerization of Ir-Ir bonds in 2D honeycomb layers of  $\text{Cu}_2\text{IrO}_3$ . We show that average valency

of Ir in Ir-Cu honeycomb layers is responsible for the theoretically predicted [40] metallicity in  $\text{Cu}_2\text{IrO}_3$  at ambient pressure, while  $\text{Cu}_2\text{IrO}_3$  is an insulator having an energy band gap of 0.3 eV (as extracted from the high  $T$  Arrhenius fit of our resistivity data). We develop this understanding by ensuring +4 oxidation state of Ir by substituting Cu in honeycomb layers with Li atoms. Our theoretical  $P\bar{1}$  structure of  $\text{Cu}_2\text{IrO}_3$  at higher pressures differs from the observed high-pressure structures, the latter having greater degree of distortions and enhanced dimerization. The pressure dependence of calculated frequency ( $\omega$ ) of Raman-active phonon modes at different pressures qualitatively agrees with observed pressure-dependent Raman spectra.

## II. EXPERIMENTAL AND COMPUTATIONAL DETAILS

High quality polycrystalline samples of  $\text{Cu}_2\text{IrO}_3$  were prepared by topotactic cation exchange reaction of  $\text{Na}_2\text{IrO}_3$  with  $\text{CuCl}$ . The samples are from the same batch as used in recent temperature-dependent Raman study [38] and the results of detailed characterization by magnetic susceptibility and muon spin resonance are reported previously [37].

High-pressure powder x-ray diffraction measurements on  $\text{Cu}_2\text{IrO}_3$  at room temperature have been performed at the XPRESS beam line ( $\lambda = 0.49585$  Å) of the Elettra Synchrotron, Trieste, Italy. Two measurement runs were performed by mounting finely ground sample in a membrane-driven symmetric diamond anvil cell (DAC): (i) run1 up to 10.7 GPa in finer pressure steps with methanol-ethanol-water (MEW) (16:3:1) as pressure transmitting medium (PTM) and (ii) run2 up to 17 GPa in larger steps with silicone oil as PTM. The 2D diffraction images were recorded on a DECTRIS PILATUS3 S 6M detector and these were converted to  $I$  vs  $2\theta$  diffraction profiles using the Dioptas software [42]. Rietveld refinements were performed for obtaining the high-pressure structural parameters using EXPGUI software [43]. For high-pressure Raman experiments, a small piece ( $\sim 150$  micron) of  $\text{Cu}_2\text{IrO}_3$  was loaded inside a Mao Bell type DAC. Solid NaCl crystal was used as the PTM rather than the ethanol+methanol mixture as the latter gave an enhanced low frequency background. Raman spectra were recorded at room temperature in a backscattering geometry using Horiba LabRAM HR Evolution Spectrometer with a DPSS laser of wavelength 532 nm and using 1.5 mW laser power. The spectra were collected by a thermoelectric cooled charge coupled device (CCD) (HORIBA Jobin Yvon, SYNCERITY 1024  $\times$  256).

High-pressure resistance measurements at low temperatures have been performed on a pressed pellet of the polycrystalline sample of  $\sim 10$   $\mu\text{m}$  thick and  $\sim 100$   $\mu\text{m}$  lateral dimensions. The resistance was measured using standard (quasi-) four probe method with suitable excitation current (depending on resistance range) and with ac lock-in detection technique. A Stuttgart version DAC was used for measurements under quasi-hydrostatic pressures up to 25 GPa using finely powdered NaCl as the PTM. The DAC was placed inside a KONTI-IT (Cryovac) cryostat. The high-pressure magnetic susceptibility ( $\chi$ ) in a dc field of 10 mT was measured in a SQUID magnetometer (S700X Cryogenic Ltd.) using nonmagnetic Cu-Be cells; a piston-cylinder cell (CamCool) for measurements up to 1.1 GPa and a DAC

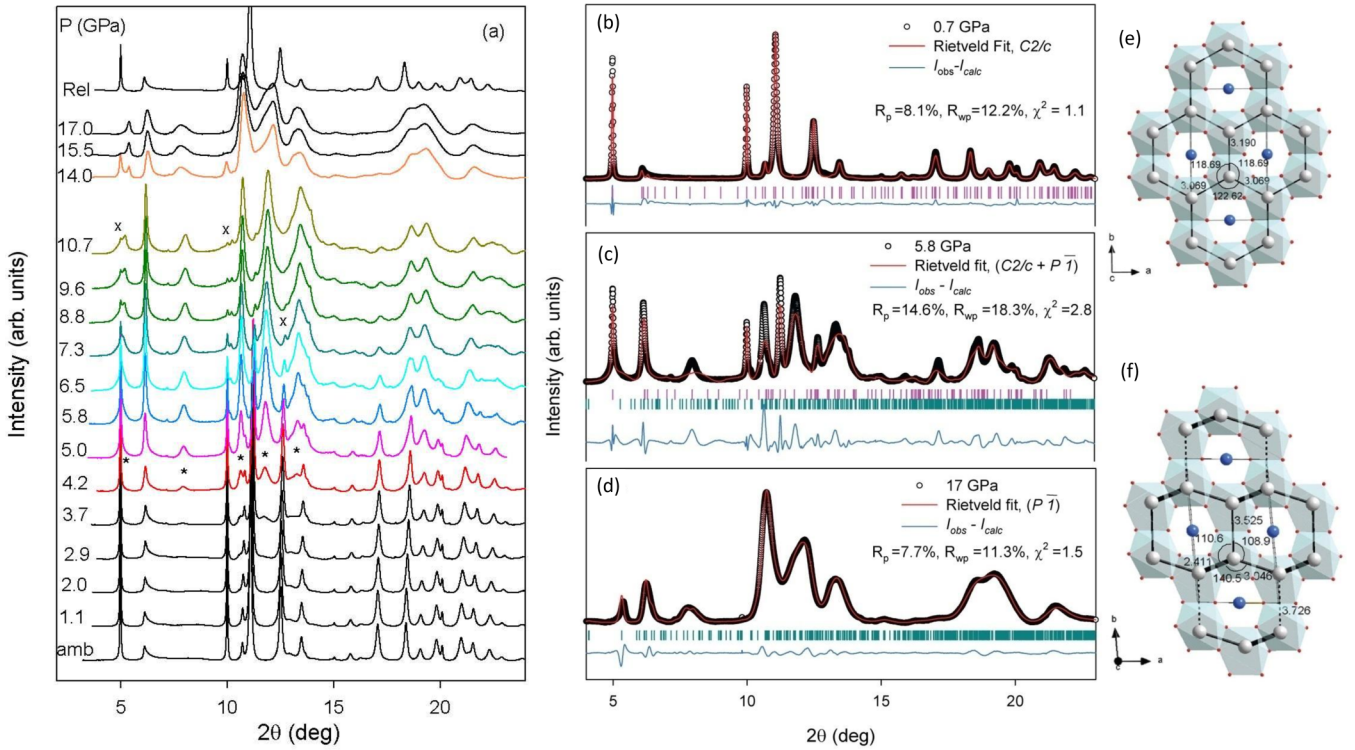


FIG. 1. (a) X-ray diffraction patterns (intensity arbitrarily shifted) of  $\text{Cu}_2\text{IrO}_3$  at various high pressures from two different runs (plots up to 10.7 GPa are with MEW as PTM and displayed patterns of higher pressures are with silicone oil as PTM). Rietveld refinement of the x-ray diffraction profiles of  $\text{Cu}_2\text{IrO}_3$  (b) at 0.7 GPa with  $C2/c$  structure, (c) at 5.8 GPa with mixed phases,  $C2/c$  and  $P\bar{1}$  structure, and (d) at 17 GPa with  $P\bar{1}$  structure. (e) Monoclinic ( $C2/c$ ) structure honeycomb layer at 0.7 GPa. (f) Distorted honeycomb layer in triclinic  $P\bar{1}$  structure at 17 GPa. The Ir-Ir bond lengths and Ir-Ir-Ir angles are labeled for both structures.

(Mcell-ultra from EasyLab) for measurements up to  $\sim 4$  GPa, with daphne oil as PTM. The thermomagnetic responses of the empty pressure cells were measured separately and subtracted from corresponding data. The pressures inside the DACs were calibrated by conventional ruby luminescence method. For  $\chi$  measurements in piston-cylinder cell, pressure was determined from the known  $P$ -dependent superconducting  $T_c$  variation of Sn [44].

Our first-principles calculations are based on density functional theory (DFT) as implemented in VASP package [45–47] and interaction between valence electrons and ions was modelled using projector-augmented-wave (PAW) potentials [48,49]. Perdew-Bruke-Ernzerhof (PBE) parametrization of exchange correlation energy functional within a generalized-gradient approximation (GGA) was used for treating electronic exchange-correlations [50,51]. An energy cut-off of 500 eV was used to truncate the plane wave basis sets used to represent Kohn-Sham (KS) wave functions. Brillouin zone (BZ) integrations were sampled on a uniform mesh of  $4 \times 2 \times 4$   $k$  points with a Gaussian smearing width of  $k_B T = 0.04$  eV. Self-consistent numerical solution of the Kohn-Sham equation was obtained iteratively to converge total energy within  $10^{-6}$  eV/cell. Structures were relaxed to minimize total energy, until magnitudes of Feynman-Hellman forces on each atom are less than  $10^{-3}$  eV/Å. In these calculations we included effects of spin orbit coupling (SOC) and on-site correlations with Hubbard- $U$  [52] parameters ( $U_{\text{eff}}$ ) 2 eV and 6.5 eV for Ir  $5d$  and Cu  $3d$  orbitals, respectively

[40]. Dynamical matrix and phonon spectrum at  $\Gamma$  point were obtained using frozen phonon method implemented in PHONOPY package [53]. SOC was not included in phonon calculations to reduce computation time. SPGLIB package [54] was used extensively to determine symmetry groups of various structures.

All the structures were visualized using VESTA [55] package and Brillouin zone was drawn using XCrySDen package [56].

### III. RESULTS AND DISCUSSION

#### A. X-ray diffraction

High-pressure x-ray diffraction measurements at room temperature show a structural phase transition of the quasi-2D honeycomb lattice compound  $\text{Cu}_2\text{IrO}_3$ . Ambient monoclinic structure (SG:  $C2/c$ ,  $z = 8$ ) is found to be stable up to  $\sim 4$  GPa, beyond which emergence of several new Bragg peaks [shown by “\*” in Fig. 1(a)] indicate occurrence of a structural phase transition, with low pressure monoclinic structure persisting up to  $\sim 15$  GPa. Also, much reduced Bragg peaks intensities of the low-pressure monoclinic phase are shown by “x” at 7.3 and 10.7 GPa in Fig. 1(a). Mixed phase patterns are shown in color. The mixed phase region in the pressure range 4–15 GPa may be described as an inhomogeneous phase with coexisting domains of  $C2/c$  and  $P\bar{1}$  structures. The structural transition is found to be completely reversible, as shown in top profile of Fig. 1(a) at  $\sim 0.1$  GPa

released from 17 GPa. Based on the diffraction pattern at 17 GPa where monoclinic phase peaks disappear completely, the high-pressure structure is indexed as triclinic (SG:  $P\bar{1}$ ,  $z = 8$ ) where atomic positions are estimated using the PowderCell software [57] and further refined by Rietveld method [43]. Figure 1 shows the Rietveld fit of the diffraction patterns in three pressure ranges: (b) monoclinic  $C2/c$  phase below 4 GPa, (c) mixed phase of monoclinic  $C2/c$  and triclinic  $P\bar{1}$  in the range of 4 to 15 GPa and (d) triclinic ( $P\bar{1}$ ) phase above 15 GPa. Because of the broadened and overlapped peaks in the triclinic phase, the mixed phase Rietveld analysis does not result in good fit (as apparent from the obtained higher  $R_{wp}$ ). Therefore, for more accurate lattice parameter determination, Le-Bail profile fitting analyses were performed without attempting to refine atomic positions. While in the low  $P$  monoclinic structure the 2D honeycomb lattice remains nearly isotropic [Fig. 1(e)], this becomes quite distorted in the high-pressure triclinic structure [with four different Ir-Ir bond lengths in the unit cell, the shortest one being  $\sim 2.41$  Å as shown in Fig. 1(f)] with possible formation of Ir-Ir covalent dimers. An enhanced structural disorder in the high-pressure triclinic phase is also apparent from the intrinsic broadened Bragg peaks compared to the monoclinic phase. The low angle ( $2\theta = 5^\circ$ ) single Bragg peaks (002) of both the phases help identifying the mixed phase range and also the  $c$ -axis collapsed nature of the triclinic structure (see Supplemental Material, SM [58]). Moreover, a strongly enhanced intensity of the  $2\theta = 6^\circ$  peak is a clear signature of heavily distorted honeycomb lattice in the triclinic phase. However, due to the inability to refine the O positions in the structural analysis of the high-pressure phase, we cannot comment on the distortion (bend/buckling) of the intralayer  $\text{IrO}_6$  octahedra and interlayer O-Cu-O dumb-bells in the high  $P$  structure.

In Figs. 2(a) and 2(b) are plotted the changes in lattice parameters of both the phases as a function of pressure. Although the monoclinic  $c1$  parameter ( $c1 = c_{\text{mono}}/2$ ) increases monotonically upon increasing the pressure, the interlayer separation remains mostly unchanged up to 4 GPa due to the increased  $\beta$  angle and decreases gradually at higher pressures (see SM [58]). The collapsed interlayer spacing in the high-pressure triclinic phase is apparent. The in-plane lattice parameters ( $a = a_{\text{mono}}$ ,  $b1 = b_{\text{mono}}/\sqrt{3}$ ) show anisotropic compression resulting in increased distortion in the honeycomb lattice up to 4 GPa, which reduces anomalously at higher pressures leading to a large distortion above 8 GPa. The monoclinic  $\beta$  angle increases monotonically up to 8 GPa and marginally decreases at higher pressures. As shown in Figs. 2(c) and 2(d), the Ir-Ir bond distances decrease by  $\sim 1\%$  up to 8 GPa, whereas the Ir-Ir-Ir bond angles increase by  $0.2$ – $0.4^\circ$  up to 4 GPa and then reach to ambient pressure values at  $\sim 9$  GPa. This implies that the high-pressure monoclinic phase is close to the regular Kitaev honeycomb lattice with reduced Ir-Ir bond distances. This along with unchanged inter-layer separation results in octahedral elongation along the trigonal axis ( $\perp$  to the  $ab$  plane) bringing this towards  $O_h$  symmetry.

High-pressure triclinic phase ( $P\bar{1}$ ) can be identified at 4.2 GPa, although with a low phase fraction (see SM [58]) causing its lattice parameters determination with large uncertainty [Figs. 2(a) and 2(b)]. At pressures above 9 GPa, with increasing phase fraction, the lattice parameters show

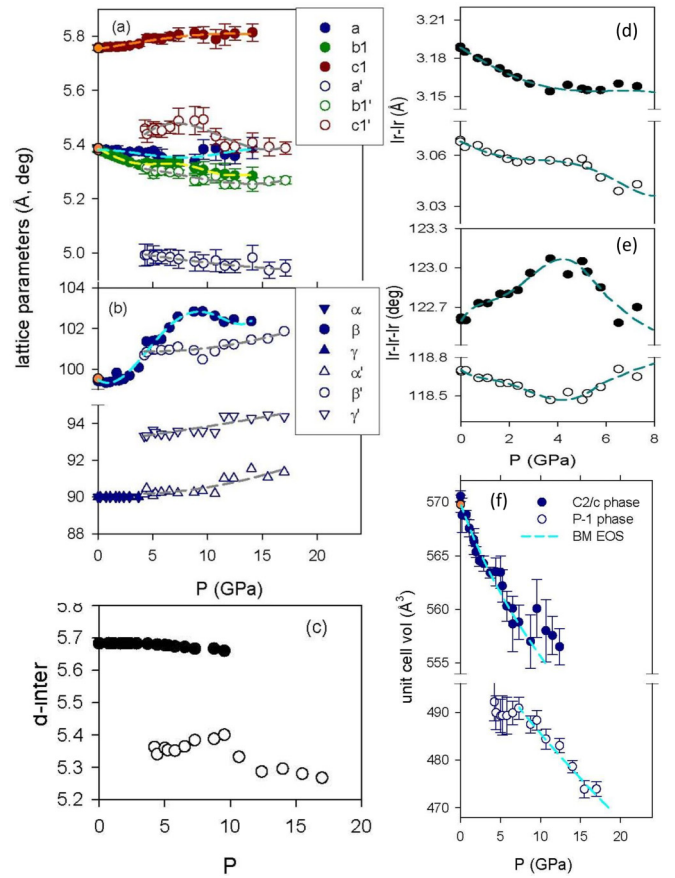


FIG. 2. [(a), (b)] Pressure dependence of the lattice constants across the structural transition. Solid symbols are for low pressure monoclinic structure ( $C2/c$ ) and open symbols (also indicated by prime legends) for high-pressure triclinic structure ( $P\bar{1}$ ). Dashed lines are guides to eye for each plot. For both structures,  $b1 = b/\sqrt{3}$  and  $c1 = c/2$ . (c) Interlayer (honeycomb) separation  $d$ -inter is plotted as a function of  $P$ . Variations of (d) Ir-Ir bond distances and (e) Ir-Ir-Ir bond angles in the low  $P$  monoclinic structure with pressure. (f) Unit-cell volume as a function of pressure in across the structural transition. Dashed cyan lines are the Birch-Murnaghan equation of state fit for both the phases (see text for details).

systematic pressure dependence. The structural transition is found to be completely reversible and the observed volume discontinuity between two phases at 9 GPa is  $\sim 12\%$ . While  $P\bar{1}$  is a direct sub-group of  $C2/c$  (hence a continuous transition is possible), the experimentally observed transition is nonetheless of first order that is apparent from the large mixed phase region and a substantial volume discontinuity at a transition pressure. The structural details of the ambient monoclinic phase and high-pressure triclinic phase at 17 GPa and at 5.8 GPa are listed in Table S1 within the SM [58].

## B. Raman scattering results

The vibrational spectra of  $\text{Cu}_2\text{IrO}_3$  for ambient  $C2/c$  monoclinic symmetry, is comprised of 39 Raman active  $\Gamma$ -point phonon modes,  $\Gamma_{\text{Raman}} = 18A_g + 21B_g$ . Among these six Raman modes at 84, 94, 510, 551, 605, and 659  $\text{cm}^{-1}$  [marked M1-M6 in Fig. 3(b)] along with a quasielastic scattering

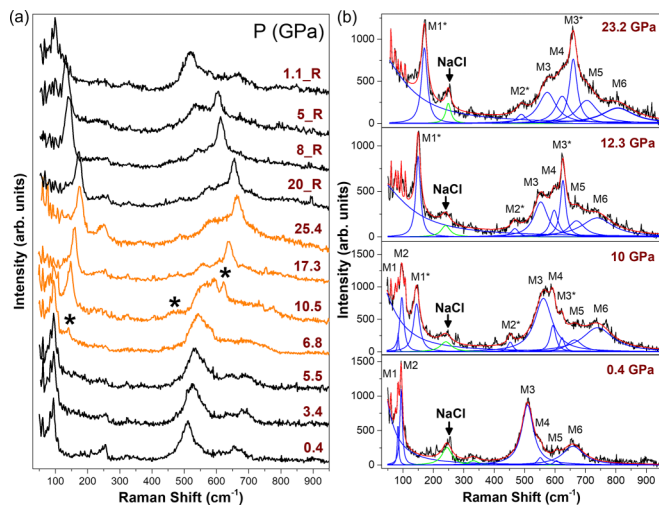


FIG. 3. (a) Raman spectra of  $\text{Cu}_2\text{IrO}_3$  at selected pressure values for pressurizing to 25.4 GPa and depressurizing (denoted by R) back to 1.1 GPa. Asterisks (\*) denote the new peaks emerging at the monoclinic to triclinic transition. (b) Phonon fits to the Raman profile at selected pressures. Black curves denote the experimental data. Individual phonon modes and the cumulative fits are shown by blue and red curves, respectively. The green curves are the NaCl peaks (used as the PTM).  $M1^*$ - $M3^*$  denote the new modes appearing in the high  $P$  structure over the existing ones ( $M1$ - $M6$ ).

(QES) background below  $150\text{ cm}^{-1}$  were observed in our ambient Raman spectrum.

Figure 3(a) portrays the pressure evolution of the Raman spectra of  $\text{Cu}_2\text{IrO}_3$  while pressurizing up to 25.4 GPa and upon decompression to 1.1 GPa. All the phonon modes including the QES signal have been fitted with Lorentzian line-shapes for the entire pressure range as shown in Fig. 3(b). The similar local symmetry of the edge-sharing  $\text{RuCl}_6$  or  $\text{IrO}_6$  octahedra of the honeycomb planes in neighbor Kitaev compounds  $\alpha\text{-RuCl}_3$  [24] and  $\alpha\text{-Li}_2\text{IrO}_3$  [13] allows qualitative assignment of the Raman modes in  $\text{Cu}_2\text{IrO}_3$ . While the low-frequency  $M1$ ,  $M2$  modes are primarily related to the vibration of the in-plane Ir network, the high-frequency  $M3$ - $M6$  modes correspond to the vibration of the  $\text{IrO}_6$  octahedra including Ir-O-Ir-O ring breathing, Ir-O-Ir-O plane shearing, and breathing of the upper and lower oxygen layers.

The ambient Raman spectral features remain unchanged under pressure up to  $\sim 6$  GPa with expected blueshift of the phonon modes beyond which the spectra show pronounced changes. At 6.8 GPa, a new mode at  $140\text{ cm}^{-1}$  (marked as  $M1^*$ ) emerges near the low frequency mode  $M2$ , while a simultaneous significant change is also noticed in the high frequency band. The weak shoulder peak  $M4$  at  $551\text{ cm}^{-1}$  starts gaining intensity significantly above this pressure. This is followed by the appearance of other two modes, one weak mode at  $457\text{ cm}^{-1}$  ( $M2^*$ ) and other at  $622\text{ cm}^{-1}$  ( $M3^*$ ) (clearly visible above 10 GPa), and disappearance of the  $M1$  and  $M2$  modes above  $\sim 11$  GPa. Appearance of new modes clearly indicates a structural transition to a lower symmetry, supporting the monoclinic to triclinic transition evidenced by our high-pressure XRD results.

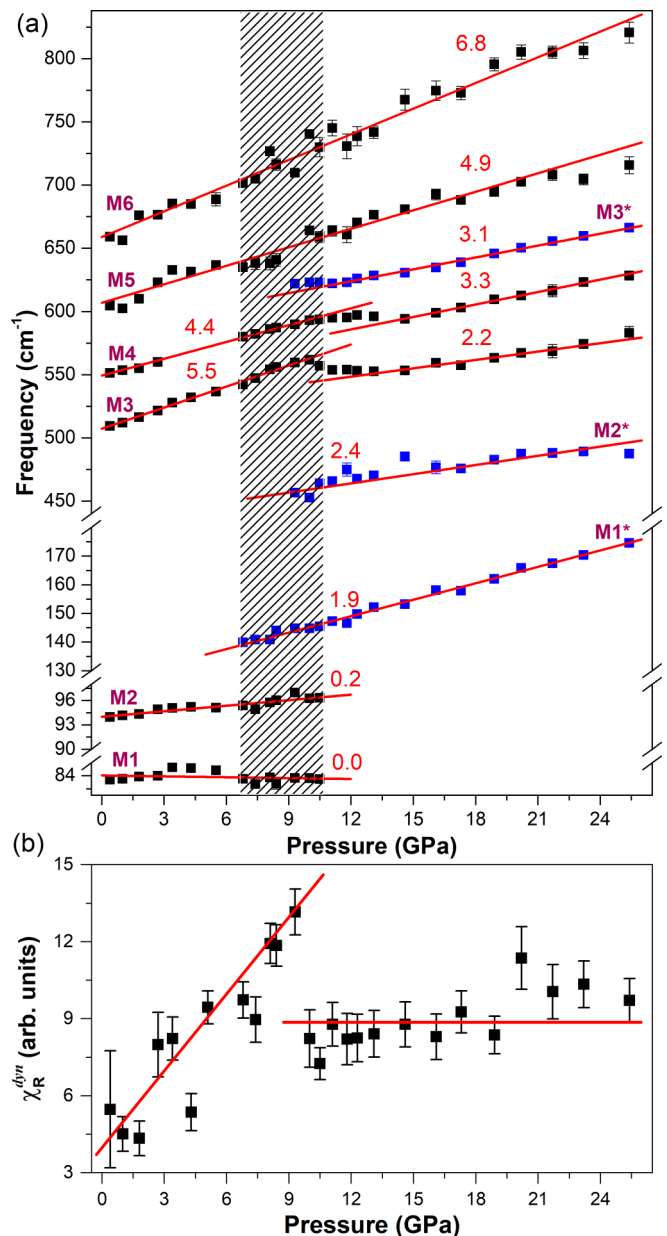


FIG. 4. (a) Pressure evolution of phonon frequencies of  $\text{Cu}_2\text{IrO}_3$ . Black squares denote the phonon modes of the low  $P$  monoclinic phase. Blue squares are the new modes appearing at the onset of the structural transition. Red-solid lines are the linear fits of phonon frequencies with pressure ( $\frac{d\omega}{dP}$  values mentioned). (b) Pressure dependence of the dynamic Raman susceptibility  $\chi_R^{\text{dyn}}$ . Red-solid lines in are guide to eyes.

The emergence of the  $M1^*$  mode ( $140\text{ cm}^{-1}$ ) at a higher frequency than that of  $M1$  and  $M2$ , indicates considerably reduced intralayer Ir-Ir bond length, consistent with the high-pressure triclinic crystal structure. The emergence of the  $M3^*$  mode and  $M4$  mode gaining intensity with pressure can be due to lifting of the degeneracy of the  $\text{IrO}_6$  vibrations due to octahedral distortion and/or symmetry breaking by the dimer formation. Upon decompression from 25 GPa, the Raman spectra regains its ambient features [Fig. 3(a)], showing reversibility of the structural transition. Figure 4(a) depicts

the pressure evolution of the mode frequencies along with linear fits. All modes exhibit expected blueshift in frequency with increasing pressure due to reduction in the unit cell volume. The M3 and M4 modes clearly show that the slopes,  $\frac{d\omega}{dP}$ , change across the structural transition. The phonon frequencies ( $\omega$ ),  $\frac{d\omega}{dP}$  values, and the corresponding Grüneisen parameters  $\gamma_i = \frac{B_0}{\omega} \frac{d\omega}{dP}$  of both the phases are listed in Table S2 within the SM [58]. The bulk moduli,  $B_0 = 203(8)$  GPa for low-pressure monoclinic phase, and  $B_0 = 208(13)$  GPa for the high  $P$  phase, are obtained from our high-pressure XRD results (see Fig. S3 within the SM [58]). The shaded region of  $\sim 7 - 11$  GPa shown in Fig. 4(a) represents the presence of the mixed phase where the new modes (M1\*-M3\*) develop gradually and above which the old M1 and M2 modes disappear. A slightly different mixed phase pressure range compared to that ( $\sim 4 - 15$  GPa) in XRD results can be attributed to different sensitivities of two probes.

Quantum spin systems with strong spin-orbit coupling often give rise to significant light scattering from the fluctuations in the spin density [59,60] resulting in quasielastic Raman response. The dynamic response from the spin system can be quantified in terms of the dynamic Raman susceptibility  $\chi_R^{\text{dyn}}$  obtained by integrating the Raman conductivity  $\frac{\chi''(\omega)}{\omega}$  using the Kramers-Kronig relation

$$\chi_R^{\text{dyn}} = \lim_{\omega \rightarrow 0} \chi(\omega, k=0) = \frac{2}{\pi} \int \frac{\chi''(\omega)}{\omega} d\omega. \quad (1)$$

The dynamic Raman tensor susceptibility  $\chi''(\omega) = \frac{I(\omega)}{n(\omega)+1}$  [ $n(\omega)$  is the Bose thermal factor] represents the imaginary part of the general susceptibility tensor  $\chi(r, t)$  [61].

Figure 4(b) illustrates the pressure dependence of the dynamic spin susceptibility  $\chi_R^{\text{dyn}}$  of  $\text{Cu}_2\text{IrO}_3$  with integration carried out from 50–1000  $\text{cm}^{-1}$  after subtracting the phonon spectra.  $\chi_R^{\text{dyn}}$  increases with pressure in the monoclinic phase (up to  $\sim 9$  GPa). We speculate that pressure-induced structural evolution towards a regular Kitaev configuration in the monoclinic phase (as discussed below) increases the fluctuations in the exchange coupled Ir spin sites resulting in the enhancement of  $\chi_R^{\text{dyn}}$ . The significant drop in  $\chi_R^{\text{dyn}}$  at higher pressures can be attributed to the reduced fluctuations (released frustration) in the distorted high-pressure triclinic structure.

### C. Magnetic susceptibility

Figure 5(a) shows zero-field-cooled (ZFC) dc susceptibility ( $\chi$ ) at ambient pressure measured using 1 T field. The  $\chi(T)$  fits well over the entire temperature range with a Curie-Weiss (CW) term and a Curie term (that becomes prominent at low temperature),

$$\chi(T) = \chi_0 + \frac{C}{(T - \Theta_{CW})} + \frac{C_{\text{imp}}}{T}. \quad (2)$$

The CW behavior indicates dominant AFM interaction ( $\Theta_{CW} = -115$  K and  $\mu_{\text{eff}} = 1.63 \mu_B$ ), while the Curie term due to defect spins becomes prominent below  $\sim 20$  K. Considering that the defect spins in  $\text{Cu}_2\text{IrO}_3$  are due to presence of mixed valent  $\text{Cu}^+/\text{Cu}^{2+}$  in the honeycomb layer (and consequently affecting a neighboring Ir atom valency and its spin configuration), it is believed that these spins may not be free

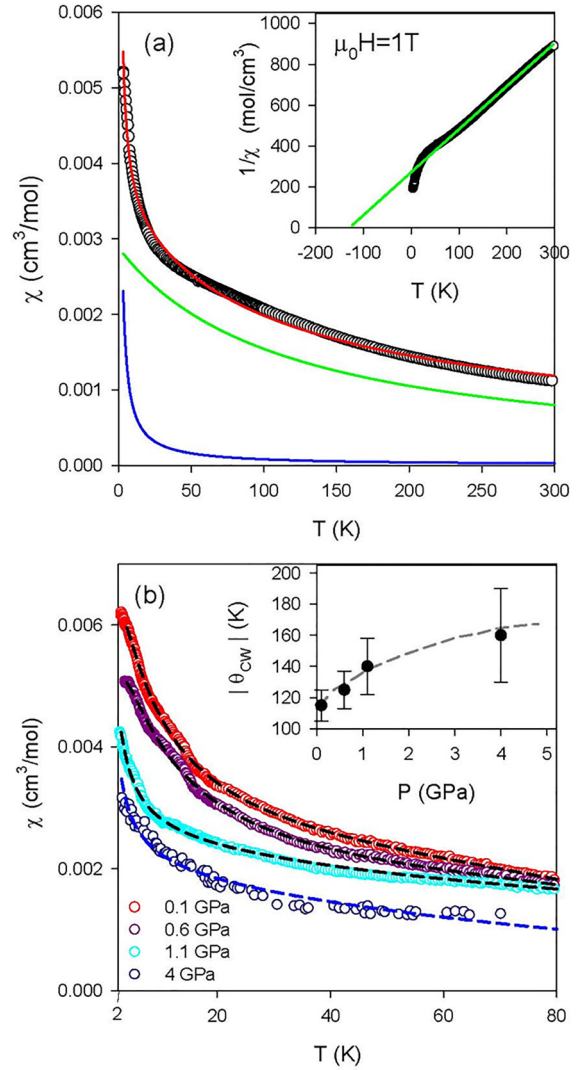


FIG. 5. (a) Zero-field-cooled dc susceptibility measured at 1 T field. The  $\chi(T)$  curve has been fitted (red-solid line) with combination of Curie-Weiss term (green line) and a Curie term (blue line) (see text). Inset:  $1/\chi$  vs  $T$  plot with linear extrapolation of  $1/\chi$  from high  $T$  (shown by green line) showing deviation from the CW law at low temperatures. (b) Field cooled susceptibility (at 10 mT field) plots as a function of temperature up to 4 GPa. The  $\chi(T)$  curves at high pressures have been fitted by two terms as in (a). The pressure variation of the CW temperature in the first term is shown as inset.

(unlike the interlayer noninteracting spins in Herbertsmithite resulting from antisite disorder [62]). Low temperature  $\chi(T)$  was thus shown previously to follow a sub-Curie fit ( $\chi = \frac{C_{\text{imp}}}{T^\alpha}$ ,  $\alpha = 0.26$ ), that was explained by bond-disordered QSL state (by the formation of random spin-singlets) as a result of the above quenched disorder [37]. Presence of defect spins at low  $T$  in our sample is also evident from the observed nonlinear  $M(H)$  at low temperatures (see SM [58]).

Magnetic properties up to 4 GPa (in the stability range of the  $C2/c$  phase) have been investigated in two arrangements: A piston-cylinder pressure cell (with 20-mg sample) for studies up to 1.1 GPa and a miniature diamond anvil cell for studies at higher  $P$ . At each pressure, empty cell background

moment was measured and subtracted carefully to obtain the sample magnetic moment. No long-range magnetic order has been detected below 100 K at high pressures. In Fig. 5(b), we plot the dc susceptibility in the  $T$  range 2–100 K at various pressures up to 4 GPa. At higher  $P$ , the overall  $\chi$  gets suppressed systematically. The  $\chi(T)$  data, fitted by Eq. (2), shows a pressure-induced systematic increase of the CW temperature [inset of Fig. 5(b)]. In absence of any magnetic ordering, this indicates that spin frustration increases with pressure in the low-pressure monoclinic phase resulting from the structural modification, as discussed later (in agreement with systematic increase of Raman dynamic susceptibility).

#### D. Electrical transport measurements

To understand the effect of pressure on the electronic properties of  $\text{Cu}_2\text{IrO}_3$  we have performed resistance measurements up to 25 GPa. In order to remove possible resistance contribution of grain boundaries, we measured room temperature resistance in three pressure cycles up to 12 GPa. While the  $R(P)$  variation in first and second cycle differ significantly, this remained almost unchanged in second and third cycle, indicating negligible grain boundary contribution in the pressure cycled sample (as shown in Fig. S6 within the SM [58]). Since at low pressures the resistance increases by six orders of magnitude at low  $T$ , a quasi four-probe measurement was performed below  $\sim 8$  GPa and standard four probe at higher pressures to improve the signal-to-noise at all pressures. The  $R(T)$  data at each pressure were collected in slow warming cycle ( $\sim 1$  K/min) to avoid thermal drift.

Figure 6(a) shows the resistance variation with temperature (1.4–300 K) on the pressure cycled  $\text{Cu}_2\text{IrO}_3$  sample (as discussed above) at various pressures. The  $R(T)$  curves remain almost unchanged up to 4.5 GPa, with systematic decrease in  $R$  at higher pressures for  $T < 50$  K. In the low pressure range  $R(T)$  obeys 3D Mott variable range hopping (VRH) conduction  $\frac{R}{R_0} = \exp[(\frac{T_0}{T})^{1/4}]$  in the temperature range 50–300 K [see Fig. 6(b)]. At low  $T$  ( $< 50$  K), a significantly reduced resistance deviating from the VRH fit can be noticed, indicating suppressed scattering channels for the charge carriers, which is yet to be understood. With increasing pressure, the increased Ir-Ir overlap enhances the carrier hopping resulting in further reduction in low temperature resistance. The Mott gap estimated from the high  $T$  Arrhenius fit ( $\sim 0.3$  eV), remains nearly unchanged up to 4.5 GPa (see the SM [58]).

At higher pressures, a conspicuous change in the  $R(T)$  can be noticed. Upon increasing pressure to 17.5 GPa, the resistance at 10 K decreases by six orders of magnitude, indicating dramatic change in its electronic structure [see inset in Fig. 6(a)]. Although the resistivity at this pressure reduces to  $\sim 10$  m $\Omega$  cm, typical for a poor metal, a non-metallic  $T$  dependence ( $\frac{dR}{dT} < 0$ ) is observed over the entire  $T$  range. With further increase of pressure, the resistance monotonically decreases with nonmetallic  $R(T)$  persisting up to 25 GPa, the highest pressure of this investigation. A similar effect of pressure on resistance has earlier been reported on its parent compound  $\text{Na}_2\text{IrO}_3$  [25,26], where rapid collapse of resistance at 4 GPa was identified with possible subtle structural modification. In  $\text{Cu}_2\text{IrO}_3$ ,  $R(T)$  above 4.5 GPa does not follow either Arrhenius or Mott VRH conduction behavior.

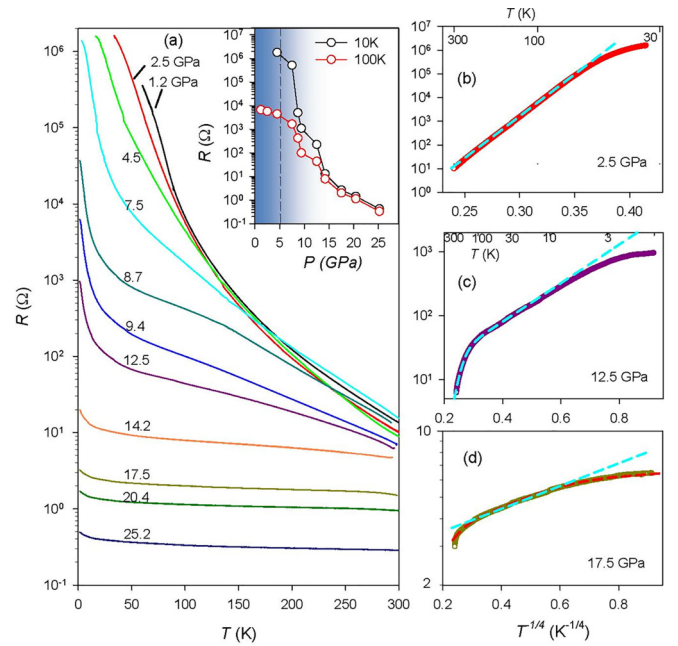


FIG. 6. (a) Semilog plot of resistance variation with temperature  $R(T)$  on the pressure cycled  $\text{Cu}_2\text{IrO}_3$  sample at various pressures. Inset shows change in sample resistance with pressure at 10 K and 100 K, resistance decreases rapidly above  $\sim 5$  GPa. Resistance plotted as a function of  $T^{-1/4}$ , and fitted curves (cyan dashed lines) with (b) 3D Mott VRH conduction term below 4.5 GPa, (c) combination of two VRH terms with two distinct  $T_0$  parameters corresponding to low  $P$  and high  $P$  phases in the  $P$  range  $\sim 5 - 15$  GPa and (d) the VRH conduction of high  $P$  phase above 15 GPa. For  $P > 15$  GPa (d), a better fit (red-dashed line) is obtained by adding a metallic conduction component with the VRH term (see main text).

Because of a clear structural transition in  $\text{Cu}_2\text{IrO}_3$  with mixed phases in 4 to 15 GPa, we attempted to explain the temperature dependence of  $R$  above 4.5 GPa using two phase model (see the SM [58]). A fit with Arrhenius conduction by invoking defect states [63] or a combination of Arrhenius and 3D VRH conduction were not successful. However, a combination of two 3D Mott VRH conduction terms with distinct energy scales,

$$\frac{1}{\rho(T)} = \sigma(T) = f\sigma_0 \exp\left[-\left(\frac{T_0}{T}\right)^{\frac{1}{4}}\right] + (1-f)\sigma_0' \exp\left[-\left(\frac{T_0'}{T}\right)^{\frac{1}{4}}\right] \quad (3)$$

( $f$  being the low-pressure phase fraction as determined from our XRD results), is seen to fit the  $R(T)$  curves well down to  $\sim 10$  K [Fig. 6(c)]. This can be understood in terms of distinct VRH energy scales  $T_0 = T_{0,\text{LP}}$  and  $T_0' = T_{0,\text{HP}}$  of the low  $P$  and high  $P$  phases and their systematic  $P$  dependence [Fig. 7(b)].

As the structural transition is completed at 15 GPa and only the high-pressure triclinic phase (with heavily distorted honeycomb lattice) is present above this pressure,  $R(T)$  plots above 15 GPa can be fit reasonably well with the second term of Eq. (3) [see the cyan dashed line in Fig. 6(d)]. However, in this pressure region,  $R(T)$  fit is found to improve significantly

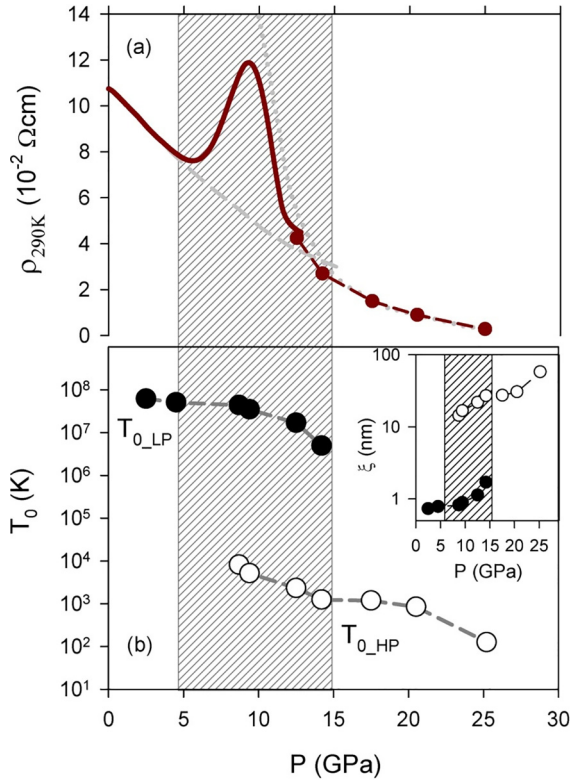


FIG. 7. (a) Room temperature resistivity of pressure cycled polycrystalline  $\text{Cu}_2\text{IrO}_3$  sample as a function of pressure. Resistance was measured while increasing  $P$  in continuous mode at a slow rate up to 13 GPa and then in larger steps up to 25 GPa. The peak shaped  $\rho(P)$  behavior in the mixed phase region can be decomposed into two  $\rho(P)$  curves (shown by dashed and dotted lines) of the two phases. (b) Variation of  $T_0$  parameters of the 3D Mott VRH conduction for two phases across the transition. Inset shows that the carrier localization lengths increase with increasing pressure in both phases (assuming unaffected DOS at  $E_f$  at high pressures).

[see red dashed line in Fig. 6(d)] (also see Fig. S8 within the SM [58]) by including metallic conduction term along with the 3D Mott VRH conduction (with energy scale  $T_{0\text{HP}}$ ),

$$\sigma(T) = \sigma_{0\text{HP}} \exp \left[ - \left( \frac{T_{0\text{HP}}}{T} \right)^{\frac{1}{4}} \right] + \sigma_0^m \left[ \frac{1}{1 + AT + BT^2} \right]. \quad (4)$$

While the VRH conduction dominates at high temperature ( $T > 50$  K), the metallic conduction takes over at lower temperatures. Note that with much reduced characteristic energy scale ( $T_{0\text{HP}}$ ) of the VRH term, the high  $P$  phase is already on the verge of metallization ( $E_a \sim 10$  meV, see Fig. S7c within the SM [58]). The inclusion of additional metallic conductivity can perhaps be justified due to the presence of  $\text{Cu}^{2+}$  defects in the honeycomb layer, adding excess density of states at the Fermi level, which gets noticeable in the high  $P$  phase [36]. It is pertinent here to note that semimetals often exhibit mixed carrier (nonmetallic and metallic) conduction [64,65].

In Fig. 7 we summarize the results of our resistance measurements. Figure 7(a) shows the plot of room temperature

resistivity  $\rho(P)$  up to 25 GPa. Upon increasing  $P$  up to  $\sim 5$  GPa (primarily in the low  $P$  phase), the  $\rho$  decreases monotonically. With the emergence of triclinic phase above this pressure,  $\rho$  first increases rapidly up to 9 GPa above which it decreases sharply. The increase of  $\rho$  above 5 GPa can be due to increased phase fraction of the high  $P$  phase (nano domains) having large resistivity. As the domains grow in size,  $\rho$  decreases rapidly above 9 GPa. The interplay between domain size, phase fraction, and intrinsic resistivity of the high  $P$  phase may result in this nonmonotonic  $\rho(P)$  in the mixed phase region.

In Fig. 7(b) are plotted the VRH  $T_0$  values (in log scale) as a function of  $P$ . The characteristic energies of the two phases ( $T_{0\text{LP}}$  and  $T_{0\text{HP}}$ ) decrease with pressure. Inset of Fig. 7(b) shows the variation of the Mott localization length ( $\xi$ ) in both phases as a function of pressure using the equation  $T_0 = \frac{21.2}{k_B \xi^3 g}$ ,  $g$  being the nonvanishing density of states at the Fermi level. Mott localization length ( $\xi$ ) has been estimated assuming  $g$  to be similar to that of ambient pressure  $\text{Na}_2\text{IrO}_3$  ( $\sim 10^{-5} \text{ eV}^{-1} \text{ \AA}^{-3}$ ) [66]. In the low  $P$  monoclinic phase,  $\xi = 0.7$  nm and  $\xi/r \sim 2$ ,  $r$  being the Ir-Ir intersite distance, indicating significant intersite hopping. For this phase,  $\xi$  starts increasing above 5 GPa. A much lower  $T_{0\text{HP}}$  of the high-pressure triclinic phase gives  $\xi = 12$  nm at 9 GPa, assuming an unchanged DOS at the Fermi level (as the disorder states may remain unaffected in the high  $P$  phase). An order of magnitude increase of the localization length clearly indicates the high  $P$  phase to be of more itinerant character. However, a significant increase of DOS may also be responsible for the reduction of  $T_{0\text{HP}}$ . While a detailed band structure calculation will certainly help to identify its origin, a much reduced  $T_{0\text{HP}}$  clearly indicates the high  $P$  phase to be close to a localized-itinerant crossover.

## E. Density functional theoretical analysis

### 1. Ground state at $P = 0$ GPa

At ambient conditions in experiment,  $\text{Cu}_2\text{IrO}_3$  occurs in the monoclinic  $C2/c$  phase [28] with 8 formula units (f.u.) per conventional unit cell. In a recent study, Fabbris *et al.* [40] showed another structure ( $P2_1/c$  with 4 f.u. per unit cell) to be also consistent with the experimental XRD pattern but lower in energy (7 meV/f.u.) than the earlier reported  $C2/c$  structure. Performing complete structural (atomic positions and lattice parameters) relaxation of both the structures ( $C2/c$  and  $P2_1/c$ ), we confirm  $P2_1/c$  to be the ground state structure with energy lower than that of the  $C2/c$  structure by an amount of 13 meV/f.u. (consistent with Ref. [40]). Our estimate of lattice parameters for the ground state structure  $P2_1/c$  ( $a = 6.00 \text{ \AA}$ ,  $b = 9.49 \text{ \AA}$ ,  $c = 5.43 \text{ \AA}$ ,  $\alpha = 90.0^\circ$ ,  $\beta = 107.9^\circ$ ,  $\gamma = 90.0^\circ$ ) agrees well with those reported earlier [40] (see SM [58] for details). As most of the Kiteave QSL candidates exist in the  $C2/c$  space group, we selected this phase for the experimental data analysis over  $P2_1/c$ . It should be noted that the two structures can be transformed into one-another by symmetry operations. They only differ in the atomic positions of one Cu atom in the  $\text{CuO}_2$  dumbbells, which lie in the interlayer honeycomb planes. However, atomic arrangement in the honeycomb layer is exactly the same in both the space groups. Therefore, these two structures cannot be uniquely

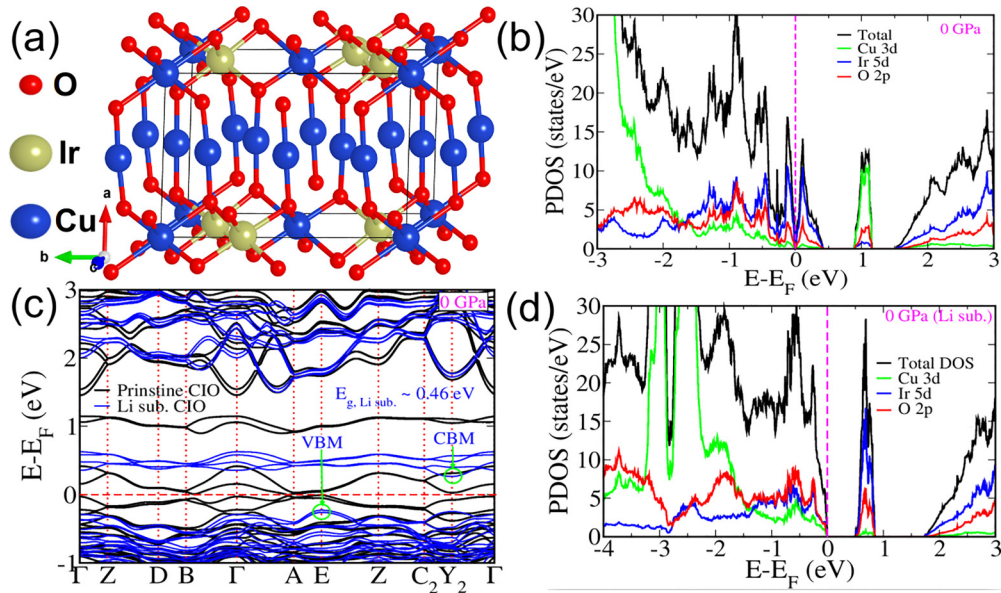


FIG. 8. (a) Conventional unit cell of  $\text{Cu}_2\text{IrO}_3$  in  $P2_1/c$  structure with 2D honeycomb layers formed by Cu-Ir atoms (see Fig. S12 within the SM [58]) and connected by O–Cu–O dumbbells. (b) Orbital projected electronic density of states of  $\text{Cu}_2\text{IrO}_3$  at 0 GPa showing metallic nature with a pseudo gap. (c) Electronic structure (see Fig. S10 within the SM [58] for high symmetry path and Brillouin zone) of pristine  $\text{Cu}_2\text{IrO}_3$  (black) and Li-substituted  $\text{Cu}_2\text{IrO}_3$  (blue) at 0 GPa. Li-substitution at honeycomb layer of  $\text{Cu}_2\text{IrO}_3$  (Cu of 2b site is substituted with Li) opens up a band gap of 0.46 eV. (d) Orbital projected electronic density of states of Li-substituted  $\text{Cu}_2\text{IrO}_3$  at 0 GPa showing insulating behavior similar to earlier reports [36].

distinguished from XRD pattern. Hence, the results of structural analysis based on  $P2_1/c$  will remain unaltered from the presented results based on the  $C2/c$  structure.

Experimentally, an electronic bandgap of  $\sim 0.3$  eV is observed in the  $C2/c$  phase of  $\text{Cu}_2\text{IrO}_3$  at  $P = 0$  GPa. In contrast, calculated electronic band structure and orbital projected electronic density of states (PDOS) at  $P = 0$  GPa (see Fig. 8) show that in  $P2_1/c$  structure  $\text{Cu}_2\text{IrO}_3$  is metallic with a pseudo gap. It is argued that metallicity arises in calculated electronic structure because the mixed valence states of Cu-Ir (Cu in  $\text{Cu}^{+2/+1}$  and Ir in  $\text{Ir}^{+4/+3}$  state) atoms [36,37] in the honeycomb layer are averaged in calculations. At  $P = 0$  GPa,  $\text{Cu}_2\text{IrO}_3$  can have an insulating ground state only if Ir (with SOC and on-site electronic correlation) is in  $+4$  oxidation state (see Ref. [67] for details). To force Ir in  $\text{Ir}^{+4}$  state, we substituted Cu atoms of the honeycomb layers with Li atoms in the optimized structure of  $\text{Cu}_2\text{IrO}_3$  [36] (Cu and Li have comparable atomic radii 132 nm and 128 nm, respectively; see Fig. S12 of SM [58]). Unlike Cu, Li exists only as  $\text{Li}^{+1}$  enforcing  $+4$  oxidation state for Ir. This rules out the possibility of average oxidation states of Cu and Ir in the honeycomb layer and thus, opens up a band gap of  $\sim 0.46$  eV comparable to its experimental value (0.3 eV). The optimized  $P2_1/c$  structure of  $\text{Cu}_2\text{IrO}_3$  has a net magnetic moment of  $2.87\mu_B/\text{cell}$  with Ir and Cu magnetic moments of  $0.16 - 0.22\mu_B$  and  $0.7\mu_B$ , respectively, which are consistent with the values reported earlier [40].

## 2. Dimerization of Ir-Ir bonds at high pressures

At ambient conditions,  $P2_1/c$  structure of  $\text{Cu}_2\text{IrO}_3$  consists of 2D honeycomb layers of Ir-Cu atoms with interlayer connectivity by O–Cu–O dumbbells (see Fig. 8 and Fig. S13

within the SM [58]).  $P2_1/c$  structure has four point symmetry operations viz., identity:  $I$ , inversion:  $i$ , screw axis  $\parallel$  to  $y$  axis:  $\{C_{2y}|0.5\ 0.5\}$ , and glide plane  $\perp$  to  $y$  axis:  $\{\sigma_y|0.5\ 0.5\}$  (numbers in the curly parenthesis denote fractional translation). Our experimental XRD pattern suggests significant dimerization of Ir-Ir bonds in 2D honeycomb layers in the high-pressure triclinic  $P\bar{1}$  phase, which breaks the glide plane  $\{\sigma_y|0.5\ 0.5\}$  and screw axis  $\{C_{2y}|0.5\ 0.5\}$  symmetries of  $P2_1/c$  phase while retaining the identity and inversion symmetries. In unconstrained (full cell) structural optimization, at high pressures ( $P > 7$  GPa),  $P2_1/c$  structure relaxes to  $P\bar{1}$  phase. Hence, it is not possible to determine the difference in enthalpies of  $P2_1/c$  and  $P\bar{1}$  structures at high pressure. This structural transition appears to be a second order phase transition (not involving discontinuous volume change). However, we find this transition is affected by a coupling of localized ordering field (like spin and dimerization) with strain [see Fig. 10(i)], and such strain-phonon coupling is well known to cause the first order character of a structural phase transition through a symmetry allowed quartic term that is negative.

Our estimates of lattice parameters and Ir-Ir bond lengths at  $P = 7$  GPa reveal (see Fig. 9) dimerization of Ir–Ir bonds. However, calculated high-pressure  $P\bar{1}$  phase differs from the experimentally observed phase at high pressures (see the SM [58] for details). While resistivity measurements show that band gap of  $\text{Cu}_2\text{IrO}_3$  reduces with increasing pressure, we find opening of an electronic bandgap after the structural transition to  $P\bar{1}$  phase, which enhances with pressure (see Fig. 10 for the pressure dependence of electronic orbital projected DOS), similar to that reported in the earlier study of Fabbris *et al.* [40]. On the other hand, calculated PDOS of Li substituted  $\text{Cu}_2\text{IrO}_3$  shows a band gap of  $\sim 0.46$  eV at  $P = 0$  GPa, which remains essentially unchanged with

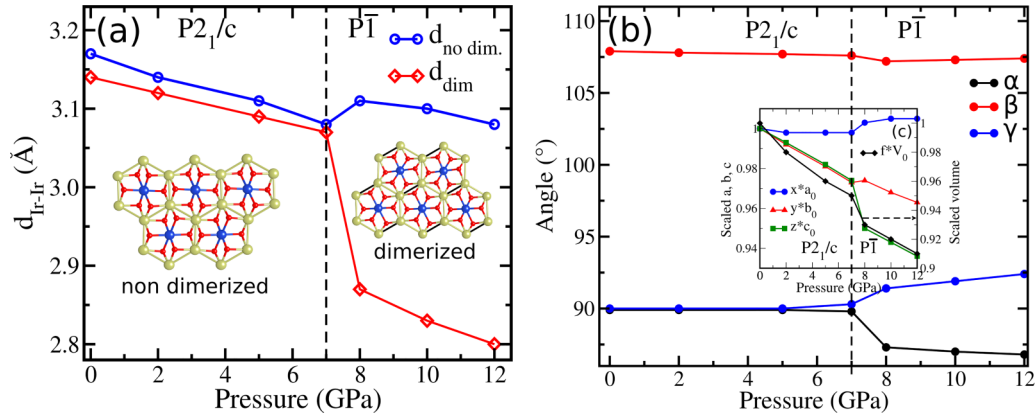


FIG. 9. (a) Pressure variation of Ir-Ir bond lengths in the honeycomb layer of  $\text{Cu}_2\text{IrO}_3$  showing dimerization of some Ir-Ir bond with pressure. after the transition to  $P\bar{1}$  at  $P \sim 7$  GPa. (b) Evolution of optimized lattice parameters  $\alpha$ ,  $\beta$ ,  $\gamma$  of  $\text{Cu}_2\text{IrO}_3$  with pressure. Inset shows pressure evolution of scaled lattice parameters (with respect to ambient  $a_0$ ,  $b_0$ ,  $c_0$ ,  $V_0$ )  $a$ ,  $b$ ,  $c$ , and volume  $V$ . The vertical-dashed lines around 7 GPa in (a) and (b) denote the boundary between the low pressure  $P2_1/c$  and high pressure  $P\bar{1}$  phases.

increase in pressure till 12 GPa (see Fig. S12 within the SM [58]). From experimental XRD pattern, we observe that Ir-Ir bond lengths at  $P = 0$  GPa have variance of  $\sim 4\%$  [Fig. 2(d)], whereas the optimized structure exhibits about 1% variance in bond lengths (Fig. 9). As we showed earlier, the band gap is sensitive to Ir-Ir bond length variance associated with mixed valence/oxidation states of Ir and Cu, this is a possible reason for the discrepancy between experimentally and theoretically obtained band gaps at  $P = 0$  GPa. The difference between the

calculated pressure dependence of band gap and experimental results is probably because of a high degree of dimerization and associated distortions in the Cu-O dumbbells due to variable valence of Ir and Cu in  $\text{Cu}_2\text{IrO}_3$ , which are absent in the optimized  $P\bar{1}$  phase at high-pressure.

As shown in Fig. 10(i), we find a significant change in total magnetic moment of  $\text{Cu}_2\text{IrO}_3$  during structural transition (involving dimerization of Ir atoms in the 2D honeycomb lattice), which reveals a strong spin-phonon coupling in the system.

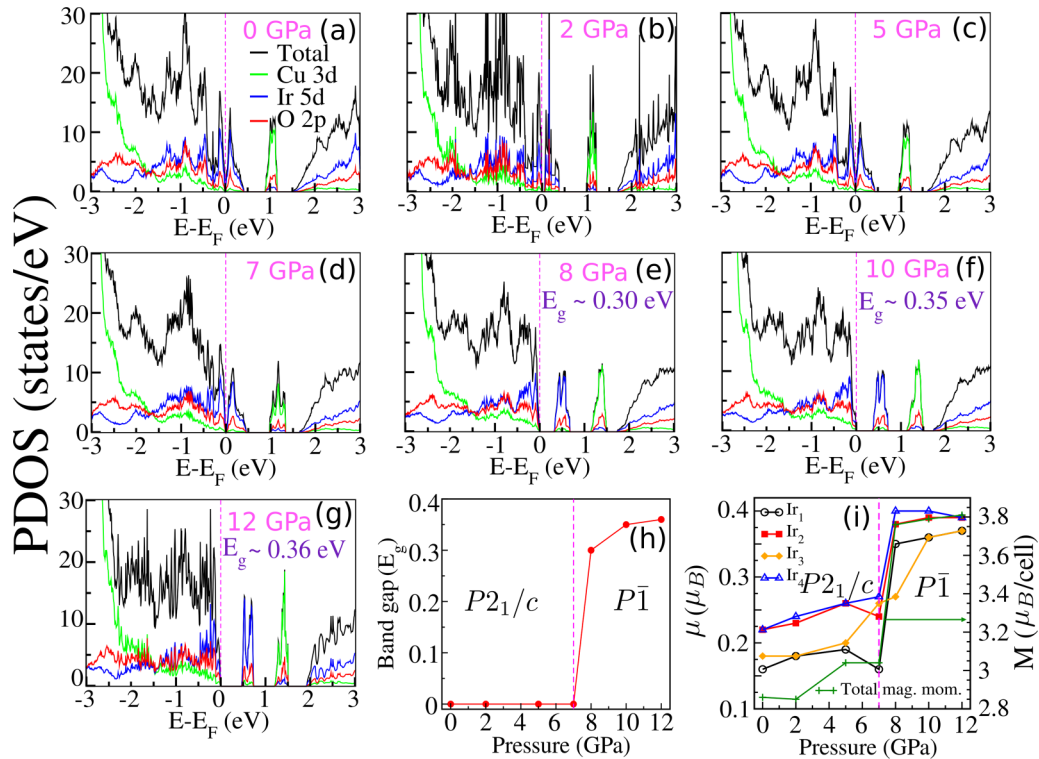


FIG. 10. Orbital projected electronic density of states of pristine  $\text{Cu}_2\text{IrO}_3$  at pressures  $P$  (a) 0 GPa, (b) 2 GPa, (c) 5 GPa, (d) 7 GPa, (e) 8 GPa, (f) 10 GPa, and (g) 12 GPa. Up to 7 GPa,  $\text{Cu}_2\text{IrO}_3$  is metallic with a pseudo-gap at Fermi level and states near the Fermi level are dominated by Ir  $5d$  orbitals. After 7 GPa, bandgap opens up and values are mentioned in the plots. (h) Pressure dependence of electronic band gap. (i) Pressure variation of total magnetic moment of  $\text{Cu}_2\text{IrO}_3$  (green) and individual moments of the four Ir atoms in the unit cell (black, red, yellow, and blue).

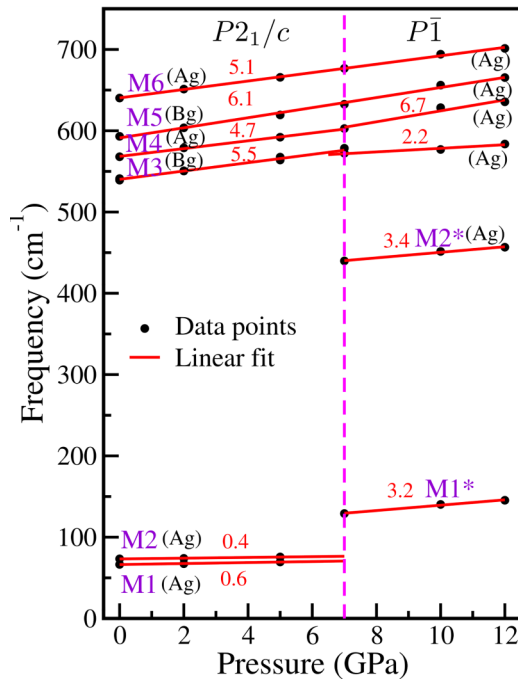


FIG. 11. Pressure variation of some of the calculated frequencies of  $\Gamma$ -point Raman-active phonon modes of  $\text{Cu}_2\text{IrO}_3$  in the low-pressure  $P2_1/c$  phase and high-pressure  $P\bar{1}$  phase. Numbers near the lines denote slopes  $\frac{d\omega}{dP}$  (mode symmetries are indicated in parentheses).

We find a notable enhancement in the magnetic moments of Ir atoms arising from change in its oxidation state to +4. This is responsible for a band gap is obtained in the calculated electronic structure of high pressure  $P\bar{1}$  phase (see the SM [58] Fig. S15 for details).

### 3. Pressure dependent Raman spectra

Frequencies of zone center phonons (calculated without inclusion of SOC) of the  $P2_1/c$  phase at  $P = 0$  GPa (see Table S8 within the SM [58] for details) confirm its dynamical stability. Our calculated  $P$  dependence of Raman active phonons (see Fig. 11) agrees qualitatively with experiment. As our calculation could not capture experimentally observed high-pressure  $P\bar{1}$  phase, our estimates of  $\frac{d\omega}{dP}$  do not quite compare well with experimentally observed values.

## IV. DISCUSSION

In the stability range of the monoclinic structure ( $C2/c$ ) of  $\text{Cu}_2\text{IrO}_3$  (for  $P < 4$  GPa), application of hydrostatic pressure does not reduce the interhoneycomb separation, whereas intralayer Ir-Ir bond length decreases by more than 1%. This reduction has no effect on the Ir-O-Ir angles in Ir hexagons, but brings the  $\text{IrO}_6$  octahedra towards ideal  $O_h$  symmetry by elongating along the trigonal symmetry axis ( $\perp ab$  plane) (see the SM [58]). This can possibly increase Kitaev exchange ( $K$ ) with respect to Heisenberg exchange [68,69]. Although an increased  $d-d$  overlap and slightly deviated Ir-Ir angles from the ideal  $120^\circ$  may increase Heisenberg exchange  $J$  (nearest neighbor and beyond), the enhanced effective  $K/J$

exchange ratio is expected to drive the system towards the Kitaev limit at higher pressures [70]. This is supported by our observed systematic increase with pressure of the CW temperature in the dc magnetic susceptibility as well as the dynamical Raman susceptibility [Fig. 4(c)]. The decrease of room-temperature resistivity with increasing pressure in the low  $P$  phase is due to increased Ir-Ir hopping as a result of the above structural modifications. In this pressure range,  $R(T)$  follows a 3D Mott VRH carrier conduction with characteristic energy scale  $T_{0LP} \sim 5 \times 10^7$  K, in agreement with other iridate compounds [26,66], that also decreases only marginally with increasing pressure [Fig. 7(b)].

At higher pressures ( $P > 4$  GPa), the system undergoes structural transition into a triclinic structure ( $P\bar{1}$ ) with heavily distorted honeycomb lattice (with four distinct Ir-Ir bond distances, shortest Ir-Ir bond length  $\sim 2.41$  Å) and with  $\sim 8\%$  decrease in interlayer separation. As the above Ir-Ir bond length is shorter than that in iridium metal, a highly covalent bond formation is expected resulting in Ir-Ir dimerization. Our XRD analysis indicate that we do not observe intermediate  $\alpha - P\bar{1}$  triclinic phase as reported by Refs. [40,41] above 7 GPa, which involves formation of Ir-Ir dimers (with two distinct Ir-Ir bonds). Rather, our observed XRD pattern of high-pressure phase agrees with the previously reported [40,41] high-pressure pattern after the second transition above  $\sim 11 - 15$  GPa ( $\alpha' - P\bar{1}$ ). Although Ref. [40] theoretically predicted the possible structures, which are inconsistent with the observed pattern, both the previous studies [40,41] were unsuccessful in indexing and refining the crystal structure of this new high pressure phase with collapsed interplanar distance. In the present paper, we have indexed this unknown structure giving detailed structural parameters. Results of our resistance measurements show that the carrier conduction in the high  $P$  triclinic phase is of Mott VRH type with much reduced energy scale ( $T_{0HP}$ ) (weak localization) compared to the low  $P$  phase, which progressively decreases on increasing pressure, thus approaching itinerant character (due to either increased localization length or enhanced DOS at the Fermi level). This can be understood in terms of band broadening at higher pressures as well as Ir-Ir covalent bond formation [25,27]. In  $\text{Li}_2\text{IrO}_3$  and  $\text{Na}_2\text{IrO}_3$ , a similar reduced resistivity has been observed at a much higher pressure (above 45 GPa). As the high-pressure phase fraction is low ( $< 50\%$ ) up to  $\sim 9$  GPa, our attempt to measure magnetic susceptibility of the high-pressure phase has not been successful. Investigation of possible ordering of bond singlets in the pure high-pressure phase suggests a need to do magnetic measurements above 15 GPa.

At further higher pressures ( $P > 15$  GPa),  $R(T)$  shows persistent nonmetallic behavior as seen in similar layered honeycomb compounds, attributed to the crossover of Mott insulator to itinerant behavior due to formation of additional states at the Fermi level [25,27]. Recently, Jin *et al.* [41] have reported insulator to metal transition above 13.8 GPa where a metallic behavior is observed with a resistance minimum at  $\sim 15$  K. Although the results of the present study on polycrystalline  $\text{Cu}_2\text{IrO}_3$  show persistent nonmetallic behavior up to 25 GPa, detailed  $R(T)$  analysis indicates possible metalization in the higher pressure triclinic structure. The different pressure dependence of  $R(T)$  curves as compared to that

reported by Ref. [41] may be attributed to different levels of  $\text{Cu}^+/\text{Cu}^{2+}$  disorder in the  $\text{Cu}_2\text{IrO}_3$  samples. The presence of mixed carrier conduction in the high-pressure triclinic phase can also be due to large pressure inhomogeneity over the sample area that demands further investigations. While persistent nonmetallic state is common in layered perovskite iridates [71],  $\text{Sr}_3\text{Ir}_2\text{O}_7$  exhibits pressure-induced anisotropic metallization [72]. A nonmetallic  $T$  dependence with significantly low resistivity can originate from such anisotropic metallization in the high-pressure phase of polycrystalline  $\text{Cu}_2\text{IrO}_3$  (with possible metallization only in honeycomb layer). Exploration in this regard requires single crystal  $\text{Cu}_2\text{IrO}_3$  (not yet available), but will be of immense help for better understanding of layered honeycomb iridates in general.

In summary, quasi-2D layered honeycomb Kitaev candidate  $\text{Cu}_2\text{IrO}_3$  undergoes pressure-induced structural phase transition (monoclinic  $C2/c \rightarrow$  triclinic  $P\bar{1}$ ) with a broad mixed phase pressure range ( $\sim 4$  to 15 GPa). The triclinic phase consists of heavily distorted honeycomb lattice with Ir-Ir dimer formation and a collapsed interlayer separation. In the stability range of the low-pressure monoclinic phase, structural evolution with hydrostatic pressure brings the system closer to Kitaev limit, as indicated by the enhanced CW temperature from magnetic susceptibility, nonemergence of long-range magnetic order and enhanced dynamic Raman susceptibility. High-pressure resistance measurements up to 25 GPa show resilient nonmetallic  $R(T)$  behavior with drastically reduced resistivity in the high-pressure phase.

A Mott variable-range-hopping conduction with much reduced  $T_0$  indicates that the high-pressure phase is close to the localized-itinerant border. Using first-principles calculations, we presented a pressure-induced structural transition in  $\text{Cu}_2\text{IrO}_3$  from  $P2_1/c$  phase to  $P\bar{1}$  phase around 7 GPa. We find that Ir-Ir bonds in the 2D honeycomb layer get dimerized in  $P\bar{1}$  phase, which is in line with our experiments. Magnetic moments are enhanced and electronic band gap opens up with such dimerization, revealing a strong spin-phonon coupling, that arises from change in oxidation state of Ir. Thus, our calculations provide evidence for interplay between oxidation state of Ir, its spin and Ir-Ir bond dimerization, fluctuations of which are probably responsible for same discrepancy between simple DFT and experiment. Our calculated  $P$ -dependence of Raman-active phonon modes agree qualitatively with the experimental Raman spectroscopy results.

#### ACKNOWLEDGMENTS

A.K.S. thanks Nanomission Council and the Year of Science professorship of DST for financial support. High-pressure PXRD investigations have been performed at Elettra synchrotron, Trieste under the proposal ID No. 20195289. A.S. is thankful to JNCASR for providing a research fellowship and computing facilities. U.V.W. acknowledges support from a J. C. Bose National Fellowship of SERB-DST, Govt. of India.

- 
- [1] A. Kitaev, *Ann. Phys.* **321**, 2 (2006).
- [2] J. Chaloupka, G. Jackeli, and G. Khaliullin, *Phys. Rev. Lett.* **105**, 027204 (2010).
- [3] S. K. Choi, R. Coldea, A. N. Kolmogorov, T. Lancaster, I. I. Mazin, S. J. Blundell, P. G. Radaelli, Y. Singh, P. Gegenwart, K. R. Choi, S.-W. Cheong, P. J. Baker, C. Stock, and J. Taylor, *Phys. Rev. Lett.* **108**, 127204 (2012).
- [4] Y. Singh, S. Manni, J. Reuther, T. Berlijn, R. Thomale, W. Ku, S. Trebst, and P. Gegenwart, *Phys. Rev. Lett.* **108**, 127203 (2012).
- [5] R. Comin, G. Levy, B. Ludbrook, Z.-H. Zhu, C. N. Veenstra, J. A. Rosen, Y. Singh, P. Gegenwart, D. Stricker, J. N. Hancock, D. van der Marel, I. S. Elfimov, and A. Damascelli, *Phys. Rev. Lett.* **109**, 266406 (2012).
- [6] D. K. Satapathy, M. A. Uribe-Laverde, I. Marozau, V. K. Malik, S. Das, T. Wagner, C. Marcelot, J. Stahn, S. Brück, A. Rühm, S. Macke, T. Tietze, E. Goering, A. Frañó, J.-H. Kim, M. Wu, E. Benckiser, B. Keimer, A. Devishvili, B. P. Toperverg *et al.*, *Phys. Rev. Lett.* **108**, 197201 (2012).
- [7] S. H. Chun, J.-W. Kim, J. Kim, H. Zheng, C. C. Stoumpos, C. D. Malliakas, J. F. Mitchell, K. Mehlawat, Y. Singh, Y. Choi *et al.*, *Nat. Phys.* **11**, 462 (2015).
- [8] R. D. Johnson, S. C. Williams, A. A. Haghighirad, J. Singleton, V. Zapf, P. Manuel, I. I. Mazin, Y. Li, H. O. Jeschke, R. Valentí, and R. Coldea, *Phys. Rev. B* **92**, 235119 (2015).
- [9] J. Nasu, J. Knolle, D. L. Kovrizhin, Y. Motome, and R. Moessner, *Nat. Phys.* **12**, 912 (2016).
- [10] S. Nishimoto, V. M. Katukuri, V. Yushankhai, H. Stoll, U. K. Röbber, L. Hozoi, I. Rousochatzakis, and J. van den Brink, *Nat. Commun.* **7**, 10273 (2016).
- [11] S. C. Williams, R. D. Johnson, F. Freund, S. Choi, A. Jesche, I. Kimchi, S. Manni, A. Bombardi, P. Manuel, P. Gegenwart, and R. Coldea, *Phys. Rev. B* **93**, 195158 (2016).
- [12] A. Revelli, M. Moretti Sala, G. Monaco, C. Hickey, P. Becker, F. Freund, A. Jesche, P. Gegenwart, T. Eschmann, F. L. Buessen, S. Trebst, P. H. M. van Loosdrecht, J. van den Brink, and M. Grüninger, *Phys. Rev. Res.* **2**, 043094 (2020).
- [13] G. Li, L.-L. Huang, X. Chen, C. Liu, S. Pei, X. Wang, S. Wang, Y. Zhao, D. Yu, L. Wang, F. Ye, J.-W. Mei, and M. Huang, *Phys. Rev. B* **101**, 174436 (2020).
- [14] L. J. Sandilands, Y. Tian, K. W. Plumb, Y. J. Kim, and K. S. Burch, *Phys. Rev. Lett.* **114**, 147201 (2015).
- [15] S. Manni, S. Choi, I. I. Mazin, R. Coldea, M. Altmeyer, H. O. Jeschke, R. Valentí, and P. Gegenwart, *Phys. Rev. B* **89**, 245113 (2014).
- [16] V. Hermann, J. Ebad-Allah, F. Freund, I. M. Pietsch, A. Jesche, A. A. Tsirlin, J. Deisenhofer, M. Hanfland, P. Gegenwart, and C. A. Kuntscher, *Phys. Rev. B* **96**, 195137 (2017).
- [17] S.-H. Baek, S.-H. Do, K.-Y. Choi, Y. S. Kwon, A. U. B. Wolter, S. Nishimoto, J. van den Brink, and B. Büchner, *Phys. Rev. Lett.* **119**, 037201 (2017).
- [18] J. Zheng, K. Ran, T. Li, J. Wang, P. Wang, B. Liu, Z.-X. Liu, B. Normand, J. Wen, and W. Yu, *Phys. Rev. Lett.* **119**, 227208 (2017).

- [19] S. D. Das, S. Kundu, Z. Zhu, E. Mun, R. D. McDonald, G. Li, L. Balicas, A. McCollam, G. Cao, J. G. Rau, H.-Y. Kee, V. Tripathi, and S. E. Sebastian, *Phys. Rev. B* **99**, 081101(R) (2019).
- [20] J. P. Clancy, H. Gretarsson, J. A. Sears, Y. Singh, S. Desgreniers, K. Mehlawat, S. Layek, G. K. Rozenberg, Y. Ding, M. H. Upton *et al.*, *npj Quantum Mater.* **3**, 35 (2018).
- [21] V. Hermann, M. Altmeyer, J. Ebad-Allah, F. Freund, A. Jesche, A. A. Tsirlin, P. G. M. Hanfland, I. I. Mazin, D. I. Khomskii, R. Valentí, and C. A. Kuntscher, *Phys. Rev. B* **97**, 020104(R) (2018).
- [22] G. Bastien, G. Garbarino, R. Yadav, F. J. Martinez-Casado, R. B. Rodríguez, Q. Stahl, M. Kusch, S. P. Limandri, R. Ray, P. Lampen-Kelley, D. G. Mandrus, S. E. Nagler, M. Roslova, A. Isaeva, T. Doert, L. Hozoi, A. U. B. Wolter, B. Büchner, J. Geck, and J. van den Brink, *Phys. Rev. B* **97**, 241108(R) (2018).
- [23] K. Hu, Z. Zhou, Y.-W. Wei, C.-K. Li, and J. Feng, *Phys. Rev. B* **98**, 100103(R) (2018).
- [24] G. Li, X. Chen, Y. Gan, F. Li, M. Yan, F. Ye, S. Pei, Y. Zhang, L. Wang, H. Su, J. Dai, Y. Chen, Y. Shi, X. W. Wang, L. Zhang, S. Wang, D. Yu, F. Ye, J.-W. Mei, and M. Huang, *Phys. Rev. Materials* **3**, 023601 (2019).
- [25] X. Xi, X. Bo, X. S. Xu, P. P. Kong, Z. Liu, X. G. Hong, C. Q. Jin, G. Cao, X. Wan, and G. L. Carr, *Phys. Rev. B* **98**, 125117 (2018).
- [26] S. Layek, K. Mehlawat, D. Levy, E. Greenberg, M. P. Pasternak, J.-P. Itié, Y. Singh, and G. K. Rozenberg, *Phys. Rev. B* **102**, 085156 (2020).
- [27] Z. Wang, J. Guo, F. F. Tafti, A. Hegg, S. Sen, V. A. Sidorov, L. Wang, S. Cai, W. Yi, Y. Zhou, H. Wang, S. Zhang, K. Yang, A. Li, X. Li, Y. Li, J. Liu, Y. Shi, W. Ku, Q. Wu *et al.*, *Phys. Rev. B* **97**, 245149 (2018).
- [28] M. Abramchuk, C. O. -Keskinbora, J. W. Krizan, K. R. Metz, D. C. Bell, and F. Tafti, *J. Am. Chem. Soc.* **139**, 15371 (2017).
- [29] K. Kitagawa, T. Takayama, Y. Matsumoto, A. Kato, R. Takano, Y. Kishimoto, S. Bette, R. Dinnebier, G. Jackeli, and H. Takagi, *Nature (London)* **554**, 341 (2018).
- [30] F. Bahrami, W. Lafargue-Dit-Hauret, O. I. Lebedev, R. Movshovich, H.-Y. Yang, D. Broido, X. Rocquefelte, and F. Tafti, *Phys. Rev. Lett.* **123**, 237203 (2019).
- [31] F. Bahrami, E. M. Kenney, C. Wang, A. Berlie, O. I. Lebedev, M. J. Graf, and F. Tafti, *Phys. Rev. B* **103**, 094427 (2021).
- [32] J. Knolle, R. Moessner, and N. B. Perkins, *Phys. Rev. Lett.* **122**, 047202 (2019).
- [33] R. Yadav, R. Ray, M. S. Eldeeb, S. Nishimoto, L. Hozoi, and J. van den Brink, *Phys. Rev. Lett.* **121**, 197203 (2018).
- [34] Y. Li, S. M. Winter, and R. Valentí, *Phys. Rev. Lett.* **121**, 247202 (2018).
- [35] S. Pei, L. L. Huang, G. Li, X. Chen, B. Xi, X. W. Wang, Y. Shi, D. Yu, C. Liu, L. W. Wang, F. Ye, M. Huang, and J. W. Mei, *Phys. Rev. B* **101**, 201101(R) (2020).
- [36] E. M. Kenney, C. U. Segre, W. Lafargue-Dit-Hauret, O. I. Lebedev, M. Abramchuk, A. Berlie, S. P. Cottrell, G. Simutis, F. Bahrami, N. E. Mordvinova, G. Fabbris, J. L. McChesney, D. Haskel, X. Rocquefelte, M. J. Graf, and F. Tafti, *Phys. Rev. B* **100**, 094418 (2019).
- [37] Y. S. Choi, C. H. Lee, S. Lee, S. Yoon, W. J. Lee, J. Park, A. Ali, Y. Singh, J. C. Orain, G. Kim, J. S. Rhyee, W. T. Chen, F. Chou, and K. Y. Choi, *Phys. Rev. Lett.* **122**, 167202 (2019).
- [38] S. Pal, A. Seth, P. Sakrikar, A. Ali, S. Bhattacharjee, D. V. S. Muthu, Y. Singh, and A. K. Sood, *Phys. Rev. B* **104**, 184420 (2021).
- [39] S. K. Takahashi, J. Wang, A. Arsenault, T. Imai, M. Abramchuk, F. Tafti, and P. M. Singer, *Phys. Rev. X* **9**, 031047 (2019).
- [40] G. Fabbris, A. Thorn, W. Bi, M. Abramchuk, F. Bahrami, J. H. Kim, T. Shinmei, T. Irifune, F. Tafti, A. N. Kolmogorov, and D. Haskel, *Phys. Rev. B* **104**, 014102 (2021).
- [41] C. Jin, Y. Wang, M. Jin, Z. Jiang, D. Jiang, J. Li, Y. Nakamoto, K. Shimizu, and J. Zhu, *Phys. Rev. B* **105**, 144402 (2022).
- [42] C. Prescher and V. B. Prakapenka, *High Press. Res.* **35**, 223 (2015).
- [43] B. H. Toby, *J. Appl. Cryst.* **34**, 210 (2001).
- [44] A. Eiling and J. S. Schilling, *J. Phys. F: Met. Phys.* **11**, 623 (1981).
- [45] G. Kresse and J. Hafner, *Phys. Rev. B* **47**, 558 (1993).
- [46] G. Kresse and J. Furthmüller, *Comput. Mater. Sci.* **6**, 15 (1996).
- [47] G. Kresse and J. Furthmüller, *Phys. Rev. B* **54**, 11169 (1996).
- [48] P. E. Blöchl, *Phys. Rev. B* **50**, 17953 (1994).
- [49] G. Kresse and D. Joubert, *Phys. Rev. B* **59**, 1758 (1999).
- [50] J. P. Perdew, K. Burke, and M. Ernzerhof, *Phys. Rev. Lett.* **77**, 3865 (1996).
- [51] J. P. Perdew, K. Burke, and M. Ernzerhof, *Phys. Rev. Lett.* **78**, 1396(E) (1997).
- [52] V. I. Anisimov, F. Aryasetiawan, and A. I. Lichtenstein, *J. Phys.: Condens. Matter* **9**, 767 (1997).
- [53] A. Togo and I. Tanaka, *Scr. Mater.* **108**, 1 (2015).
- [54] A. Togo and I. Tanaka, [arXiv:1808.01590](https://arxiv.org/abs/1808.01590)
- [55] K. Momma and F. Izumi, *J. Appl. Crystallogr.* **44**, 1272 (2011).
- [56] A. Kokalj, *J. Mol. Graph. Model.* **17**, 176 (1999).
- [57] W. Kraus and G. Nolze, *J. Appl. Cryst.* **29**, 301 (1996).
- [58] See Supplemental Material at <http://link.aps.org/supplemental/10.1103/PhysRevB.107.085105> for additional results from powder x-ray diffraction, magnetic susceptibility, high pressure resistance measurements, and DFT calculations.
- [59] G. F. Reiter, *Phys. Rev. B* **13**, 169 (1976).
- [60] P. Lemmens, G. Guntherodt, and C. Gros, *Phys. Rep.* **375**, 1 (2003).
- [61] M. G. Cottam and D. J. Lockwood, *Light Scattering in Magnetic Solids* (Wiley-Interscience, New York, 1986).
- [62] P. Malavi, S. Pal, D. V. S. Muthu, S. Sahoo, S. Karmakar, and A. K. Sood, *Phys. Rev. B* **101**, 214402 (2020).
- [63] W. Schnelle, B. E. Prasad, C. Felser, M. Jansen, E. V. Komleva, S. V. Streltsov, I. I. Mazin, D. Khalyavin, P. Manuel, S. Pal, D. V. S. Muthu, A. K. Sood, E. S. Klyushina, B. Lake, J.-C. Orain, and H. Luetkens, *Phys. Rev. B* **103**, 214413 (2021).
- [64] G. Xu, W. Wang, X. Zhang, Y. Du, E. Liu, S. Wang, G. Wu, Z. Liu, and X. X. Zhang, *Sci. Rep.* **4**, 5709 (2014).
- [65] O. Pavlosiuk, D. Kaczorowski, and P. Wiśniewski, *Sci. Rep.* **5**, 9158 (2015).
- [66] J. Rodriguez, G. Lopez, F. Ramirez, N. P. Breznay, R. Kealhofer, V. Nagarajan, D. Latzke, S. Wilson, N. Marrufo, P. Santiago, J. Lara, A. Diego, E. Molina, D. Rosser, H. Tavassol,

- A. Lanzara, J. G. Analytis, and C. Ojeda-Aristizabal, *Phys. Rev. B* **101**, 235415 (2020).
- [67] B. J. Kim, H. Jin, S. J. Moon, J.-Y. Kim, B.-G. Park, C. S. Leem, J. Yu, T. W. Noh, C. Kim, S.-J. Oh, J.-H. Park, V. Durairaj, G. Cao, and E. Rotenberg, *Phys. Rev. Lett.* **101**, 076402 (2008).
- [68] B. H. Kim, G. Khaliullin, and B. I. Min, *Phys. Rev. B* **89**, 081109(R) (2014).
- [69] S. M. Winter, Y. Li, H. O. Jeschke, and R. Valentí, *Phys. Rev. B* **93**, 214431 (2016).
- [70] R. Yadav, S. Rachel, L. Hozoi, J. van den Brink, and G. Jackeli, *Phys. Rev. B* **98**, 121107(R) (2018).
- [71] C. Chen, Y. Zhou, X. Chen, T. Han, C. An, Y. Zhou, Y. Yuan, B. Zhang, S. Wang, R. Zhang, L. Zhang, C. Zhang, Z. Yang, L. E. DeLong, and G. Cao, *Phys. Rev. B* **101**, 144102 (2020).
- [72] Y. Ding, L. Yang, C.-C. Chen, H.-S. Kim, M. J. Han, W. Luo, Z. Feng, M. Upton, D. Casa, J. Kim, T. Gog, Z. Zeng, G. Cao, H. k. Mao, and M. van Veenendaal, *Phys. Rev. Lett.* **116**, 216402 (2016).